HHS Public Access

Author manuscript

Int J Hyperthermia. Author manuscript; available in PMC 2015 December 30.

Published in final edited form as:

Int J Hyperthermia. 2015 June ; 31(4): 359–374. doi:10.3109/02656736.2015.1005178.

Magnetic nanoparticle hyperthermia enhances radiation therapy: A study in mouse models of human prostate cancer

Anilchandra Attaluri[1], **Sri Kamal Kandala**[2], **Michele Wabler**[1], **Haoming Zhou**[1], **Christine Cornejo**[1], **Michael Armour**[1], **Mohammad Hedayati**[1], **Yonggang Zhang**[1], **Theodore L. DeWeese**[1], **Cila Herman**[2], and **Robert Ivkov**[1]

[1]Department of Radiation Oncology and Molecular Radiation Sciences, Johns Hopkins University School of Medicine, Baltimore, Maryland [2]Department of Mechanical Engineering, Johns Hopkins University, Baltimore, Maryland, USA

Abstract

Purpose—We aimed to characterise magnetic nanoparticle hyperthermia (mNPH) with radiation therapy (RT) for prostate cancer.

Methods—Human prostate cancer subcutaneous tumours, PC3 and LAPC-4, were grown in nude male mice. When tumours measured 150 mm^3 magnetic iron oxide nanoparticles (MIONPs) were injected into tumours to a target dose of 5.5 mg Fe/cm^3 tumour, and treated 24 h later by exposure to alternating magnetic field (AMF). Mice were randomly assigned to one of four cohorts to characterise (1) intratumour MIONP distribution, (2) effects of variable thermal dose mNPH (fixed AMF peak amplitude 24 kA/m at 160±5 kHz) with/without RT (5 Gy), (3) effects of RT (RT5: 5 Gy; RT8: 8 Gy), and (4) fixed thermal dose mNPH (43 °C for 20min) with/without RT (5 Gy). MIONP concentration and distribution were assessed following sacrifice and tissue harvest using inductively coupled plasma mass spectrometry (ICP-MS) and Prussian blue staining, respectively. Tumour growth was monitored and compared among treated groups.

Results—LAPC-4 tumours retained higher MIONP concentration and more uniform distribution than did PC3 tumours. AMF power modulation provided similar thermal dose for mNPH and combination therapy groups (CEM43: LAPC-4: 33.6 ± 3.4 versus 25.9 ± 0.8, and PC3: 27.19 ± 0.7 versus 27.50 ± 0.6), thereby overcoming limitations of MIONP distribution and yielding statistically significant tumour growth delay.

Conclusion—PC3 and LAPC-4 tumours represent two biological models that demonstrate different patterns of nanoparticle retention and distribution, offering a model to make comparisons of these effects for mNPH. Modulating power for mNPH offers potential to overcome limitations of MIONP distribution to enhance mNPH.

Correspondence: Robert Ivkov, David H. Koch Cancer Research Building, Room 442, Department of Radiation Oncology and Molecular Radiation Sciences, Johns Hopkins University School of Medicine, 1550 Orleans Street, Baltimore, MD 21231, USA. Tel: 443-287-7282. Fax: 410-502-2821. rivkov1@jhmi.edu.

Declaration of interest

R. Ivkov is an inventor on several issued and pending patents that disclose nanoparticle formulations for imaging and hyperthermia. All patents on which R. Ivkov is an inventor are assigned to either Johns Hopkins University or Aduro Biotech. All other authors report no conflicts of interest.

Keywords

Hyperthermia; magnetic nanoparticles; prostate cancer; radiation therapy; radiosensitiser

Introduction

Prostate cancer persists as a major contributor to mortality in men [1,2]. Clinical definitions of high-risk disease vary, and choosing among available treatment options remains challenging because aggressive therapy, i.e. radical prostatectomy, high-dose external-beam radiotherapy (RT), hormone ablation, or brachytherapy carry significant risks to the patient [1–4]. For definitive prostate cancer treatment (as with most other cancers), adequate therapy to tumour–tissue boundary or 'margin' is a primary concern. Disease recurrence is considered more likely with inadequate treatment of the tumour margin; however, preserving normal tissue to maintain quality of life and reducing treatment-related morbidity compel clinicians to minimise exposure or resection of tissue near the margins. Thus, for radiation therapy, achieving a uniform dose throughout the tumour volume is less important than ensuring a minimum therapeutic dose is achieved throughout the tumour, particularly at the tumour–tissue margins. Combining radiation therapy with agents that enhance therapeutic effect is an approach that offers potential benefits because lower radiation doses can be effective, thus also reducing toxicity.

Hyperthermia or heating tissues to a temperature within the range 41–46 °C enhances the potency of radiation depending upon thermal dose (time at temperature) [5–9]. Magnetic nanoparticle hyperthermia (mNPH) has received increasing attention as a potential 'new frontier' in cancer medicine [10,11]. Hyperthermia with magnetic iron oxide nanoparticles (MIONPs) and alternating magnetic fields (AMFs) requires targeted deposition of MIONPs inside the tumour, followed by application of AMFs, causing the particles to heat [12]. This heat conducts into the area immediately surrounding the particles and if a modestly elevated temperature is maintained in the tumour for sufficient time tumour cells are destroyed or damaged, thus enhancing effectiveness of additional agents. Magnetic nanoparticle-mediated hyperthermia or mNPH has held appeal for over 50 years because of the potential to deposit focal, tumourspecific heating while simultaneously minimising heating of surrounding normal tissue [13]. Indeed, such potential to limit damage to nearby sensitive neural structures, such as in brain, prostate, and spinal cord tissues has motivated preclinical and clinical development [14–24]. The success of mNPH, as with other thermal therapies, depends therefore upon surmounting the challenges to efficiently target tumours and to achieve the appropriate heat distribution.

Combined hyperthermia and radiation therapy generally enhances management of locally advanced and recurrent cancers. For mNPH, a central issue is the extent to which intratumour nanoparticle distribution limits the thermal profile, and to identify limitations for nanoparticle deposition [10,17]. Response to hyperthermia depends critically upon thermal dose, defined as 'time at temperature', deposited to the tumour [25]. More specifically, the lowest thermal dose achieved anywhere in the tumour will determine the response [25,26]. Uniform thermal dose throughout the tumour is not an explicit

requirement of therapy to achieve favourable response. Rather, the goal of hyperthermia (as with radiotherapy) is to achieve at least a minimum effective dose in >90% of tumour volume, particularly at the tumour–tissue margins while minimising thermal dose to normal surrounding tissue. For mNPH, therefore, the tissue concentration and distribution of MIONPs (heat sources) are critical parameters. This reveals the paradox of mNPH: the small size of the nanoparticles enables their tissue and cell penetration, but this also removes control of precise tissue localisation that may be necessary for reliable therapy. On the other hand, the variable heat output (loss power) of MIONPs which depends upon AMF amplitude and frequency, can afford non-invasive and dynamic control of the thermal dose. We can then ask whether such adjustments can be sufficient to adequately manage the thermal dose for a variety of nanoparticle distributions. Furthermore, we may consider this in the context of achieving adequate thermal dose within the tumour, but minimising energy deposition outside the tumour. Variation of MIONP heat output as an explicitly controlled parameter to achieve specific thermal dose, particularly at the tumour–tissue margin in order to spare normal adjacent tissues, has not been systematically described for mNPH.

Mode of MIONP administration affords some ‘generalised’ choice for tumour deposition. Vascular (venous or arterial) modes of (image-guided) peri-tumour delivery have been explored, with modest success [27–29]. In this case, nanoparticle distribution depends in a complex way on vascular network and fluid flow. Nanoparticle distribution within tumour following intratumour or percutaneous injection, however, is dictated by injection parameters (e.g. injection rate, volume, solution viscosity) and by tumour physiological and mechanical properties (e.g. interstitial pressure, tissue density, stromal content, vascularity), only some of which can be controlled by the investigator. It is thus the topic of significant debate that mNPH can have only limited clinical utility because (1) tumour targeting with MIONPs is difficult; and (2) percutaneous delivery produces unpredictable and inconsistent intratumour nanoparticle distribution. The former abrogates successful clinical translation because too little material is deposited into tumours for beneficial effect, whereas the latter produces variable thermal dose, precluding prescriptive planning and effective treatment. Ideally, robust treatment scenarios should be sought that yield necessary tumour damage for a range of particle distributions likely to be encountered in clinical practice.

In this study we sought to explore the effects of nanoparticle-mediated heat delivery as a potential therapeutic modality with radiation in which nanoparticle heat output and tissue distribution were varied. We measured temperature and effects on tumour growth delay of mNPH±RT following percutaneous delivery of MIONPs into two mouse models of prostate cancer that consistently demonstrated different MIONP concentration and distribution between them. The two tumour models were derived from human prostate cancer cells lines LAPC-4 and PC3. While the tumours generated from these cell lines proved useful for comparative experiments of mNPH with respect to MIONP distribution, the cell lines also displayed different sensitivity to heat and radiation that were recapitulated in the tumour models, thus introducing a confounding element for interpretation of results. Computational models (2-dimensional) were used to elucidate relationships between nanoparticle distribution, heat output, and resulting temperature evolution in a model tumour to enhance understanding of temperature distributions that are experimentally inaccessible. We identify nanoparticle power output as a critical parameter for mNPH that can be used to compensate

for variable nanoparticle distribution in the context of combined therapy. Our results suggest that if the goal of mNPH is to achieve a minimum effective thermal dose at the tumour margin (tumour–tissue boundary), and simultaneously minimise overheating the surrounding normal tissue then power modulation with probe placement at the tumour–tissue boundary is sufficient to achieve the desired outcome in the context of underlying tumour biology. MIONPs generate hysteresis heating when exposed to AMFs that depends in part on the amplitude of the AMF. Modulating the AMF amplitude (i.e. power) can overcome the limitations created by variable nanoparticle distribution. This finding provides supporting data to motivate further exploration of nanoparticle distribution and mNPH in various models presenting varied and challenging structures.

Materials and methods

In vitro

Cell culture—Human prostate cancer cell lines, PC3 and LAPC-4, were used. PC3 cells were purchased from the American Type Culture Collection (ATCC, Manassas, VA). LAPC-4 cell line was obtained from the laboratory of R.E. Reiter (University of California, Los Angeles) under a material transfer agreement. PC3 cells were cultured in RPMI1640 medium supplemented with 10% fetal bovine serum and 2mM L-glutamine. LAPC-4 cells were cultured in Iscove's modified Dulbecco's medium (IMDM) supplemented with 10% fetal bovine serum, 2mM L-glutamine, and 1mM R1881. All cells were kept in a humidified incubator at 37 °C with 5% CO_2.

Water bath hyperthermia—A digital water bath (Model 282, Precision Instrument, Kennesaw, GA) with a maximum temperature setting of ~95.0°C and precision of 0.1 °C was used for hyperthermia. Flask and water bath temperatures were measured using two Type-T thermocouples (Omega Engineering, Stamford, CT) connected to a portable data logger (OM-DAQPro-5300, Omega Engineering). Thermocouples were calibrated with a precision certified thermometer (T-3750/64CFC, Miller and Weber, Ridgewood, NY) prior to the water bath experiments. One thermocouple was immersed directly into the water bath and another was inserted into a surrogate flask containing the same amount of medium (5 mL) as the flasks to be treated. The temperature readings of the thermocouples were recorded digitally using computer software.

Cells were exposed to four temperatures 37 °C, 40 °C, 42 °C and 43 °C for 60 minutes with 37 °C as control. Flasks were partially immersed in the water bath and water was added to the water bath to adjust the level to be slightly above the level of the culture media. To prevent contamination, flasks were secured tightly and sealed with Parafilm. Time was recorded when the flask temperature reached ± 0.5 of the target temperature.

Radiation—A Gammacell 40 137Cs irradiator (Best Theratronics, Ottawa, ON) was used for radiation treatments at room temperature. Five radiation doses (2 Gy, 4 Gy, 6 Gy, 8 Gy, and 10 Gy) were selected and compared to 0 Gy control.

Clonogenic survival assay—After each treatment cells were re-suspended and diluted to the appropriate number then plated in triplicate onto 10-cm culture dishes. At 10–14 days

after treatment, cells were stained with a solution of 0.2% crystal violet in 50% methanol and 50% distilled water. Colonies consisting of at least 50 cells were counted. The surviving fraction was determined relative to control at 37 °C or 0Gy.

Magnetic iron oxide nanoparticles (MIONPs)

Bionised nanoferrite (BNF)-starch (catalogue no. 10-00–102) nanoparticles were obtained from micromod Partikeltechnologie (Rostock, Germany) and used as received. Their mean hydrodynamic diameter was 108 nm and with a polydispersity index (PI) of 0.33 as provided by the manufacturer. Synthesis, structure, magnetic, heating, and imaging properties of these particles have been extensively described [21,22,30–33].

Mice and nanoparticle injection

The mice were housed in an Association for Assessment and Accreditation of Laboratory Animal Care-accredited facility in compliance with the *Guide for the Care and Use of Laboratory Animals* [34]. All procedures were approved by the Johns Hopkins Institutional Animal Care and Use Committee.

A total of 113 male (4–6 weeks old) athymic BALB/c nu/nu mice (Harlan Labs, Indianapolis, IN) weighing ~24±2g on a normal diet *ad libitum* and under pathogen-free conditions were used in this study. To generate PC3 tumours, 3×10^6 PC3 cells suspended in 0.1 mL of phosphate-buffered saline (PBS) were injected subcutaneously into the right thigh of each mouse. Subcutaneous LAPC-4 tumours were generated in a similar manner, using 5×10^6 LAPC-4 cells suspended in a (1:1) mixture of 0.1 mL of PBS and Geltrex™ reduced growth factor basement membrane matrix (Invitrogen A1413202, Grand Island, NY).

Mice were randomly divided into two main groups corresponding to constant power ($n = 42$) or power-modulated hyperthermia ($n = 46$), and further by tumour within each of these groups – PC3 or LAPC-4. Within each of these main tumour groups, mice were further randomly divided into subgroups corresponding to treatment – radiation therapy (RT), mNPH, and mNPH + RT. Tumour growth was measured. Time to reach 4-fold initial volume (t_0 = time at treatment) was the chosen end point in all but six mice selected from the constant power PC3 tumour group. These mice were selected for intratumour thermometry and were euthanised at the end of treatment. A schematic of the *in vivo* experimental design is provided in Figure 1(A).

A subset of 25 mice bearing PC3 ($n = 9$) and LAPC-4 (n=16) tumours were used to characterise nanoparticle distribution and retention. All mice in this cohort were sacrificed on ‘day 0’ shown in Figure 1(A).

Tumour volume was estimated from caliper measurements in three orthogonal dimensions and assuming hemi-ellipsoid geometry – V = Length × width × height × 0.5236 prior to injections. When tumours measured 150±30 mm^3 for LAPC-4 and 150 ± 50 mm^3 for PC3 the pre-determined volume for treatment, mice were anaesthetised for injections and treatments. For tumours receiving MIONP injections, BNF MIONP suspension was injected into three sites, having triangular configuration, of the tumour, with approximately 1/3

volume into each, to achieve a total delivered dose of MIONPs equalling 5.5 mg Fe/cm^3 of tumour. Saline (PBS) or BNF particles were injected in control mice (tumours) using similar methods and approximately similar volumes.

Intratumour MIONP characterisation – histopathology and ICP-MS

At 24 h after MIONP or saline injections, chosen to allow sufficient time for nanoparticle diffusion throughout the tumour, mice selected for intratumour iron characterisation were euthanised and tumours were harvested. Tumours were either fixed in formalin for histopathology or they were processed for iron quantification by inductively coupled plasma mass spectrometry (ICP-MS). Formalin-fixed tumours were sectioned and stained with Perls' reaction to qualitatively assess distribution of BNF MIONPs (i.e. ferric, Fe^{3+}) following previously described methods [35].

ICP-MS was used to quantify intratumour iron concentration to assess MIONP retention. Tumours were processed following previously described methods [35]. Briefly, each tissue sample was lyophilised, weighed, and transferred to a 7-mL Teflon microwave digestion vessel (Savillex, Eden Prairie, MN), and was suspended in nitric acid (HNO_3) for digestion in a MARS5 Xpress microwave (CEM, Matthews, NC). Samples were digested using a two-stage ramp to temperature method and the digests were diluted for analysis in an Agilent 7500ce inductively coupled plasma mass spectrometer (Agilent Technologies, Santa Clara, CA). Total iron content of each sample was calculated based on an eight-point calibration curve, blank correction, and the recovery of a standard reference material, SeroNorm Trace Elements, SERO (Billingstad, Norway). For samples having values measuring below the analytical limit of detection, one half of the limit of detection was substituted. Table 1 provides a summary of relative injected and recovered Fe from tumours.

Alternating magnetic field system

The AMF system has been previously described [36]. A water jacket, also previously described, was inserted into the induction coil and used to maintain the body temperature of the anaesthetised mice close to physiological range when exposed to AMF [37]. A photograph displaying the experimental set-up (AMF system, water jacket, chiller, and temperature probes) is shown in Figure 1(B).

Briefly, the AMF system comprised three main components: a power supply, an external impedance matching network, and a modified solenoid coil [37]. The power supply is a 120-kW induction heating system manufactured by PPECO (Watsonville, CA) that provides an alternating current to a resonant circuit with variable frequencies (135– 440 kHz). The external impedance match network (AMF Life Systems, Auburn Hills, MI) was adjusted for stable oscillation at 155 ± 10 kHz. Within the solenoid, a polypropylene jacket, through which distilled water was circulated, provided a thermal barrier to heat generated directly by the solenoid [37]. Prior to experiments, the magnitude of the magnetic field was measured at the centre of the solenoid using a magnetic field probe for several power settings to provide calibration for all studies.

Constant power mNPH

For mNPH, each anaesthetised mouse was placed into a holder constructed from a standard polypropylene 50-mL conical centrifuge tube that was positioned in the centre of the modified solenoid coil and water jacket [37]. Treatment duration was 20 min for either control (0 kA/m) or mNPH (24 kA/m peak amplitude) groups. Higher amplitude mNPH is desirable in studies with mice to simulate the effects of off-target heating resulting from eddy currents. Mice present a significantly smaller radius and volume of tissue than do humans, and thus much less eddy current heating will be generated. To compensate, higher AMF amplitudes are needed to produce off-target heating as would be encountered in a clinical setting. From the PC3 tumour-bearing mice, six were chosen for thermometry. A single AMF compatible fibre-optic temperature sensor (FISO Technologies, Quebec, Canada) was inserted into the tumour (with the tip at the approximate centre of the tumour) of each of the six randomly selected animals to measure intratumour temperatures at 1-s intervals. These animals were used only for thermometry and not for tumour growth end points. Conversely, in seven randomly selected mice bearing LAPC-4 tumours thermometry was performed on the tumour surface. These same individuals were used for tumour growth comparisons.

Power modulated mNPH and RT

Mice were randomly assigned to control (BNF MIONP only), mNPH (HT: 43.5° ± 0.5 °C), RT (RT5 or RT8), or RT5 + HT groups. Four AMF-compatible fibre-optic temperature probes were used in each mouse to measure rectal, (intra) tumour (probe tip in the approximate centre of the tumour), skin of thigh contralateral to tumour, and water jacket temperatures for each mouse. Mice comprising the AMF-sham groups were injected with BNF MIONPs and were placed in the water jacket for 20 min with AMF 0 kA/m. For the mNPH (HT) AMF amplitude was modulated to achieve an intratumour target temperature of 43.5° ± 0.5 °C. Total AMF exposure was 20 min. The water jacket temperature was dynamically adjusted to maintain the rectal temperature to between 35–39 °C. For all mice receiving combined mNPH and RT, mNPH preceded RT. For RT, mice were treated using the Small Animal Radiation Research Platform (SARRP) [38]. Tumours were irradiated with a circular beam having a 1-cm diameter. Mice were monitored for tumour growth.

Thermal dosimetry

Temperature data obtained from mNPH treatments were normalised to convert a temperature–time curve to an equivalent time at 43 °C (CEM43) using the expression provided by Sapareto et al.: CEM43 = $tR^{(43-T)}$; where t (s) is the time of treatment, T is the average temperature during the desired interval of heating, and R is a constant which is equal to 0.5 for T>43 °C and is equal to 0.25 when T<43 °C [39].

Computer simulation: thermal model

Two 2D computational thermal models were created to represent a tumour and surrounding healthy tissue. Since nanoparticle distributions in tumours vary, we used this computational phantom to analyse two extreme cases of nanoparticle distributions, to better understand the physics of the system. The tumours contained either (1) uniform or (2) concentrated

distribution of nanoparticles (Figure 1C). Both models contained an identical total number of nanoparticles and differed by nanoparticle distribution. In the uniform distribution model, the nanoparticles are evenly distributed throughout the tumour area to the tumour–tissue boundary. In the concentrated model nanoparticles are concentrated in only 40% of the tumour area extending from its centre (Figure 1C). The healthy tissue and tumour were modelled as circles with radii r_{tissue} = 9.5 mm and r_{tumour} = 4.5 mm, respectively. The model dimensions were chosen to ensure that the temperature at the outer edge of (healthy) tissue can be assumed to be at constant body temperature T = 37°C [40]. Heat transfer produced by the nanoparticles throughout either tumour or tissue was modelled by the Pennes' bioheat equation [41]

$$\rho_n c_n \frac{\partial T_n}{\partial t} = k_n \nabla^2 T_n + \rho_b c_b \omega_{b,n} (T_b - T_n) + Q_{m,n} + Q_p \quad (1)$$

where n and b represent tissue (tumour, n = 1; healthy n = 2) and blood parameters, respectively. For either tumour or healthy tissue, ρ_n, c_n, k_n, T_n, $Q_{m,n}$ denote the density, specific heat, thermal conductivity, local temperature, and metabolic heat generation rate. Correspondingly for the blood, ρ_b, c_b, ω_b, T_b denote density, specific heat, perfusion rate, and temperature, respectively. Thermophysical properties for healthy tissue, tumour, and blood are summarised in Table 2 [42–47]. Q_p denotes the total power generated by nanoparticles in each tumour. The nanoparticles are modelled as line heat sources with uniform heating strength. As a consequence, the total power generated within each of the model tumours is identical, in order to highlight differences in temperature distribution resulting from the two nanoparticle distributions.

At the interface between healthy tissue and tumour, conservation of heat flux and continuity of temperature conditions are applied. Summarised, the boundary conditions are as follows.

$$k_{tissue} \left. \frac{\partial T_{tissue}}{\partial r} \right|_{r=r_{tumour}} = k_{tumour} \left. \frac{\partial T_{tumour}}{\partial r} \right|_{r=r_{tumour}} \quad (2)$$

$$T_{tissue}(r=r_{tumour}, t) = T_{tunour}(r=r_{tumour}, t), \quad (3)$$

$$T(r=r_{tissue}) = 37^{\circ}\mathrm{C} \quad (4)$$

The governing equations (Equation 1) with the boundary conditions (Equation 2–Equation 4) were solved numerically using COMSOL Multiphysics 4.4, a commercially available finite element solver. A grid size dependency study was carried out to ensure that calculated temperatures were sufficiently independent of a chosen model grid size. When the grid size was changed from coarse (14,747 triangular elements) to fine (29,804 triangular elements), the number of elements nearly doubled, yet the calculated temperature along the radius of the tumour changed by less than 0.01%, indicating our chosen model parameters have negligible influence from grid size. A similar comparative analysis was performed to determine whether calculated temperatures were affected by the chosen time step for the transient heating process. When the time step was increased from 0.2s to 1 s, the change in

calculated temperatures was negligible (<0.001%). The model results were validated by comparing the transient temperature profiles along the radius of the tumour with the analytical solution given by Andra et al. [47]. Satisfactory agreement between analytical and numerical solutions was observed, confirming the general validity of our model.

Simulations in this study were conducted to approximate constant power and power-modulated nanoparticle hyperthermia experiments for qualitative comparison. Thermophysical properties of tissues and blood were held constant for all simulations (Table 2). To approximate constant power heating, Q_p (=4.6 × 10^5W/m^2) was fixed for a simulated duration of 60 min. The total heating power was chosen to limit the maximum temperature in the tumour to <47 °C.

To simulate power-modulated nanoparticle hyperthermia, the heating power of the nanoparticles ($Q_p(T)$) was varied with computed temperature at a specific intratumour location (T_{probe}) as the feedback control parameter. This was given by Equation 5.

$$Q_p(T) = \begin{cases} 9.2 \times 10^5 W/m^3, & \text{if} T_{probe} \leq 43.5^\circ\text{C} \\ 0.92 \times 10^5 W/m^3, & \text{if} T_{probe} > 43.5^\circ\text{C} \end{cases} \quad (5)$$

The chosen temperature reference to control power input was 43.5 °C because it is the minimum (break-point) temperature considered clinically relevant for hyperthermia treatment of human cells from *in vitro* measurements [25,26,39]. To investigate the influence of temperature probe placement on the total thermal dose, three virtual temperature probe locations – (1) centre of tumour, (2) halfway between tumour centre and tumour–tissue boundary, (3) at the tumour–tissue boundary – were considered in the computational simulation as control points. Heating with modulated power was carried out for 60 min and the temperature distributions in both tumour and healthy tissues were obtained at the end of 60 min of heating.

Statistical methods

A Kaplan–Meier survival analysis (GraphPad PRISM version 6.0 for Windows) was performed assuming time required for tumour volume to reach 4× volume at treatment time (t_0) as the ('survival') end point and log-rank (Mantel-Cox) test was used to compare between control and treated groups. A tumour growth delay (mean time to 4x tumour volume) comparison between groups was performed using a *t* test with unequal variance. Standard statistical significance scheme was used to report the comparisons between the groups (NS = $p > 0.05$; *$p \leq 0.05$; **$p \leq 0.01$; ***$p \leq 0.001$; ****$p \leq 0.0001$). Errors reported were standard error of mean.

Results

In vitro

Sensitivity to radiation and heat exhibited by PC3 and LAPC-4 cells was assessed *in vitro* with clonogenic assay to provide a baseline comparison of potential differences in response to these agents without confounding factors inherent in *in vivo* studies. The ability of

damaged cells to replicate, which correlates with their ability to effectively repair damage, was assessed following exposure to heat at varying temperatures for 60 min or varying doses of ionising radiation (25). LAPC-4 cells demonstrate significantly decreased survival when exposed to ionising radiation than do PC3 cells (Figure 2A). Similarly, LAPC-4 cells are more susceptible to the effects of hyperthermia, which is most pronounced with 60-min exposure at 43 °C. At this dose the measured surviving fraction is reduced by 100-fold relative to untreated controls, whereas PC3 cell survival is reduced only modestly (30–40% relative to controls), as shown by the solid bars in Figure 2(B). When 60-min of hyperthermia is combined with 5Gy radiation, the surviving fraction of both PC3 and LAPC-4 cells is diminished further, demonstrating a combined effect that is at least additive. Again, LAPC-4 cells demonstrate a significantly greater sensitivity to the combined therapy than do PC3 cells (Figure 2B, hashed bars). Compared to untreated controls, the surviving fraction of LAPC-4 cells exposed to 43 °C (CEM43 60) + 5Gy is about 100-fold lower (~0.03%) than the surviving fraction of similarly treated PC3 cells (~1%).

MIONP distribution and retention

Prussian blue stained tissue sections showed contrasting intratumour nanoparticle distribution for LAPC-4 and PC3 tumours (Figure 3). Inductively coupled plasma mass spectrometry (ICP-MS) analysis of the PC3 (n = 7), and LAPC-4 (n=10) tumours injected with PBS (control) or 5.5 mg Fe/cm^3 tumour showed variable MIONP retention. Recovered total iron from PC3 tumours was 55 ± 13% of injected dose, whereas for LAPC-4 tumours it was 79 ± 6% of total Fe injected (Table 1). For comparison, the measured Fe in tumour samples injected with PBS was 8 ± 2 μg Fe for LAPC-4 (n = 5) and 11 ± 1 μg Fe for PC3 (n = 3). Average total recovered mass of Fe following MIONP injection for LAPC-4 (n = 5) and PC3 (n = 4) were 830 ± 16 μg Fe and 771 ± 36 μg Fe respectively, which depended upon the measured tumour volume at the time of study. A summary of these results is provided in Table 1.

Constant power mNPH

Temperatures were measured in randomly selected individuals from both PC3 (n = 6) and LAPC-4 (n = 7) groups during constant power mNPH. For constant power mNPH, the AMF amplitude was fixed (24 kA/m) for the duration of treatment (20min), thus thermometry only provides some information of temperatures achieved. Temperature probe placement (for single-point measurements) can influence the estimated thermal dose, although actual thermal dose is unknown and independent of the measurement because AMF power is fixed. A representative temperature–time plot (PC3 tumour) is shown in Figure 4(A), demonstrating increasing tumour heating for the duration of AMF exposure.

Measured maximum PC3 intratumour temperatures are reported in Table 3. The mean maximum temperature obtained from these results is 49 ± 2 °C, where the variance is represented by standard error of the mean (95% confidence limits). Estimated values of CEM43 based on the single-point temperature measurements are also provided in Table 3 (second column). CEM43 calculations are invalid when measured temperatures exceed 49 °C because extensive tissue necrosis typically occurs, although extent of tissue necrosis was not characterised in the present study [25]. Similarly, data obtained from LAPC-4 tumours

are displayed in Table 4. Mean maximum temperature measured at the LAPC-4 tumour surface was 43 ± 1 °C, and the corresponding estimated (mean) CEM43 was 48 ± 25 (Table 4, column 2).

LAPC-4 tumours responded favourably to constant power mNPH alone with seven out of nine (77%) showing measurable response (growth delay) compared to untreated controls. Conversely, only three out of eight (38%) PC3 tumours demonstrated measurable response compared to controls. Tumour growth results are summarised in Figure 4(B) and (C). Of the responders from the PC3 group, 2 out of 3 demonstrated a complete response, i.e. no measurable tumour following treatment.

A Kaplan–Meier survival analysis was performed assuming time required for tumour volume to reach 4× volume at treatment time (t_0) as the ('survival') end point and log-rank (Mantel-Cox) test was used to compare between control and treated (24 kA/m) groups (Figure 4B and C). When compared against the untreated control, constant power mNPH was associated with a borderline significant tumour growth delay ($p = 0.055$) for LAPC-4 while PC3 showed no significant tumour growth delay ($p = 0.093$), see Figure 4(B). Median survival in the LAPC-4 control group was 21 days, whereas for the mNPH group it was 37 days giving an estimated therapeutic ratio of ~1.8 (37/21), Figure 4(C). Conversely, constant power mNPH had only a modest effect on PC3 tumour growth. Median survival of mice bearing PC3 tumours was 17 days following mNPH (20 min at 24 kA/m) whereas untreated control median survival was 14 days giving a therapeutic ratio of ~1.2 (17/14).

Power modulated mNPH and RT

Modulating both AMF power and water jacket temperature enables control of both tumour thermal dose and effects of off-target heating. A representative temperature-time plot is shown in Figure 5(A). Estimated values of CEM43 based on single-point thermometry were similar for mNPH and RT + mNPH groups (LAPC-4: 34 ± 3 and 26 ± 1, respectively), and for PC3: 27 ± 1 and 28 ± 1, respectively) with amplitude modulation. For LAPC-4 tumours, all radiation and hyperthermia treatments demonstrated statistically significant ($p<0.05$) response when compared to untreated control (Figure 5B and D). Median survival for control cohort was 21 days; and for all therapy groups it was HT: 30 days ($p<0.05$), RT5: 30 days ($p<0.05$), HT + RT5: 55 days ($p<0.01$), RT8: 47 days ($p<0.01$) (Figure 5B). Mean time to achieve a 4-fold increase of initial (t_0 = time at treatment) volume of tumours was 30 ± 4 days following HT and 29 ± 3 days for RT5, compared to 20 ± 2 days for untreated controls. The difference between times for HT and RT5 is statistically significant. Both mNPH (HT) of CEM43 ~30 and RT of 5 Gy thus produce a measurable and similar response. By contrast, a similar thermal dose has little effect on PC3 tumour growth (Figure 5C and E), which is also less than the (more modest) response due to 5Gy radiation. Combination therapy, mNPH + RT (HT at CEM43 ~30 + 5 Gy) produced improved response in both tumour models compared to control or mono-modal treatment cohorts – time to 4-fold tumour volume increase was 57 ± 4 days ($p = 0.0042$ compared with RT5) for LAPC-4, although the effect was significantly less pronounced in PC3 tumours 22 ± 2 days (a certain trend toward significance $p = 0.08$ was suggestive) for PC3 (Figure 5B – E). Interestingly, the combination therapy performed slightly better in LAPC-4 tumours than a higher dose of

8Gy RT (RT8; median survival 55 versus 47 days), although this difference was not statistically significant ($p = 0.25$). We estimate a treatment enhancement ratio ~1.6 if we assume response to RT5 + mNPH was equivalent to RT8 (Figure 5D). This is a stark contrast to response by PC3 tumours which demonstrated improved response to RT5 + mNPH compared with RT5, but not when compared against RT8 (Figure 5E).

Temperature profiles obtained from simulations comparing idealised uniform (with nanoparticles uniformly distributed throughout 'tumour' area, Figure 1C, top) with concentrated (nanoparticles at 'tumour' centre extending to 40% of tumour volume, Figure 1C, bottom) MIONP distributions for 60 min heating with constant power ($Q_p = 4.6 \times 10^5$ W/m^3) are shown in Figure 6A and B. In both cases, a temperature gradient within the tumour is predicted, which results from heat generated by MIONPs that conducts throughout the tumour and dissipates into the surrounding tissue. Temperatures calculated at the tumour boundary with respect to time for the two models are shown in Figure 6(C). Steady- state is achieved rapidly, within about 300 s for both models, although the tumour-tissue interface temperature achieved by a uniform MIONP distribution is predicted to be slightly higher (T = 40.9°C) than that achieved by a concentrated MIONP distribution (T = 40.6°C). Heat flux (loss) at the tumour–tissue interface (heating of healthy surrounding tissue) is also predicted to be greater for the uniform distribution (656 W/m^2) than for concentrated MIONP distribution (592 W/m^2).

Modulating power with computed temperature as the feedback control parameter ($Q_p(T)$) produces different temperature profiles within the tumour depending upon both MIONP distribution and control temperature probe placement (Figure 7A and B). Temperature gradients produced within a tumour bearing a uniform MIONP distribution are similar to those produced by constant power heating, although the steady-state temperature achieved at the tumour–tissue boundary is determined by placement of the temperature sensor used in the control algorithm described by Equation 5. Similarly, power-modulated heating with a concentrated MIONP distribution produces similar temperature gradients within the tumour as with constant power heating. Power-modulated heating with temperature monitoring at the tumour–tissue interface, however achieves identical steady-state temperature at the tumour boundary for both concentrated and uniform MIONP distributions. By contrast, placement of temperature probes in either the tumour centre or halfway between centre and boundary for concentrated MIONP distribution limits heating significantly more than for uniform MIONP distribution (Figure 7C and D).

Discussion

Clinical management of cancer continues to be challenged by locally advanced and high-grade disease. For prostate cancer, aggressive therapy offers benefits but the associated risks complicate treatment decisions to minimise the adverse impact of treatment-related morbidity while maintaining effective disease control [1–4]. High-dose radiation therapy is generally effective, but the potential for extensive damage to surrounding tissues often triggers careful examination of alternatives to reduce morbidity and preserve a patient's quality of life [2]. Agents that enhance the potency of radiation therapy (RT) are thus

generally beneficial because they offer the potential to reduce risks without jeopardising treatment benefit.

Biological damage resulting from hyperthermia can complement DNA damage produced by ionising radiation, making hyperthermia an attractive tool for clinical management of many cancers [5–9,25,26]. We have characterised the effects of ionising radiation and heat (without nanoparticles) on two human prostate cancer cell lines, PC3 and LAPC-4. Such a baseline comparison is useful to provide context for analysis of results obtained with xenograft models generated from these lines. LAPC-4 cells are androgen sensitive and possess mutated BRCA2 that increases their sensitivity to radiation damage, presumably by inhibiting effective homologous recombination of damaged DNA [6,8,48,49]. By contrast, PC3 cells are androgen insensitive, possess wild-type BRCA2 (although mutated p53) and display significantly less radiation sensitivity than do LAPC-4 cells at doses >3 Gy, see Figure 2(A) [48–50]. Interestingly, LAPC-4 cells are also more sensitive to heat and its combination with radiation, displaying 100-fold reduced survival when 5 Gy is combined with a 60-min exposure at 43 °C relative to untreated controls. Krawczyk et al. [6] reported that BRCA2 degradation or knockout is associated with increased radiation or heat sensitivity, but not with further increased sensitivity to combined radiation and hyperthermia. The observed heightened sensitivity of LAPC-4 cells to combined radiation and hyperthermia thus merits further study to elucidate the role of additional pathways.

Clinically, important parameters for successful cancer therapy with hyperthermia include intratumour temperature, temperature distribution, and duration of treatment (time at temperature). The accepted metric for thermal dosimetry is the cumulative equivalent minutes (duration of exposure) normalised to the base effective temperature of 43 °C (CEM43). The temperature distribution within the tumour is typically measured by T90 values which describe the temperature achieved or exceeded in 90% of the tumour area [25,26,39,51]. When combined with the base dosimetry (CEM43) to yield CEM43T90, this measure of thermal dosimetry is a superior indicator for therapeutic outcome over temperature alone [25,26,39,51]. Achieving a minimal effective dose in 90% of the tumour volume is thus the goal of therapy, and not homogeneity of thermal dose throughout the tumour volume. Minimal dose requirements, however, are often not achieved in preclinical or clinical settings because of (1) equipment providing insufficient control of energy deposition, (2) inadequate thermometry, or (3) because feedback control that incorporates thermometry with energy delivery is unavailable. Thus, despite the biological rationale and clinical demonstrations supporting hyperthermia, significant technical challenges to deliver, measure, and control heat delivery persist and inhibit widespread application.

Magnetic iron oxide nanoparticles (MIONPs) offer potential advantages for cancer hyperthermia. The generally favourable biocompatibility, small size, and responsiveness to magnetic fields of MIONPs make them suitable for many biomedical applications [10]. MIONPs, having appropriate magnetic properties, can generate substantial heat when exposed to alternating magnetic fields (AMFs) [12]. Hyperthermia with MIONPs or magnetic nanoparticle hyperthermia (mNPH) has thus been actively pursued for over 50 years, culminating in recent preclinical and clinical demonstrations of its utility for cancer imaging and therapy [10–24,51–60]. There is, however no systematic study validating the

utility of conventional dosimetry (i.e. CEM43) for nanoparticle-based thermal therapies. As this technology continues to advance to the clinic, such validation will be necessary. Intratumour MIONP concentration and distribution are generally considered critical parameters for mNPH because MIONPs are the source of heat. While MIONPs offer new potential for hyperthermia because they can deposit interstitial or intracellular heat, new challenges become evident. MIONP delivery to tumours and control of MIONP distribution within tumours present significant challenges. For locally advanced and confined disease, the former can be addressed by percutaneous delivery, often with imaging guidance similar to current clinical practice with chemotherapeutic drugs for many unresectable cancers. This mode of delivery, however, fails to completely address the issue of MIONP distribution within the tumour.

Assuming adequate delivery (i.e. MIONP concentration), the varied biology and physiology of cancer tumours places significant limitations on achievable MIONP distribution. Further, the small size and ‘fluidic’ nature of MIONP suspensions enhances potential for MIONP redistribution during and after mNPH [18,52–58]. It may thus be unrealistic to expect that nanoparticle distributions can be controlled or managed to achieve ‘idealised’ or uniform MIONP distributions consistently in preclinical or clinical settings. On the other hand, mNPH provides adjustable parameters that may enable one to compensate for these limitations.

Zones of locally high MIONP concentration are often observed within tumours following percutaneous administration [18,52–54]. Consistent with the reported examples, we observe heterogeneous iron distribution in both PC3 and LAPC-4 tumours 24h after injecting BNF suspensions into three sites of each tumour (Figure 3). Notably, we observed that the local iron deposits extend throughout LAPC-4 tumours, whereas MIONP retention seems confined to only specific regions of PC3 tumours. The latter observations are consistent with those reported by Attaluri et al. [54] who noted that fissures or ‘cracks’ can form in PC3 tumours during fluid injection, thereby providing channels for MIONP fluid flow producing a concentrating effect and preventing widespread diffusion. In a clinical setting, similar intratumour nanoparticle inhomogeneity was observed and attributed to variations of administration methods [55]. By comparing two different biological (xenograft) models of human prostate cancer with comparable administration methods, we have demonstrated significant differences between the models for intratumour nanoparticle retention and distribution. Remarkably, LAPC-4 tumours seem to present significantly different properties leading to different MIONP distribution that warrant further investigation. We also note that overall iron (MIONP) retention varies among individual tumours within each type studied, with LAPC-4 tumours consistently retaining more MIONPs measured by Fe content analysis with ICP-MS (Table 1).

Predictably, constant power heating (i.e. AMF amplitude is constant) will generate more total heat in tumour regions retaining higher MIONP concentrations, and the local temperature will increase rapidly within zones containing MIONPs when heating commences. Extending beyond the MIONP-containing zones, temperature rapidly declines leading to sharp thermal gradients [61–64]. The size or volume of these heat generating zones dominate thermal gradients in their vicinity during the initial stages of heating. Heat

generated conducts throughout the tumour away from these zones at a rate proportional to r^3, where r is the distance from the heating zone. Conversely, the rate of heat transfer across the tumour–tissue boundary depends upon the surface area of the tumour (i.e. rate $\propto r^2$) thus favouring local concentrations of MIONPs, provided the volume of heat generating zones and power meet minimum threshold values [65]. If we assume constant perfusion, heat flux at the tumour–tissue boundary is thus higher for a uniform distribution of particles than for concentrated particles, potentially increasing thermal damage to surrounding sensitive tissues and contributing to under-treatment within the tumour. Therefore, decreasing the volume of heat generation zone(s) below a critical value that depends upon the total tumour volume becomes unfavourable for effective therapy because heat flux across the tumour–tissue boundary exceeds the rate of heat deposition within the tumour necessary to sustain a therapeutic thermal gradient. Following the initial steep rise in temperature, a steady state is achieved, depending upon the duration of heating, resulting in a thermal gradient within the tumour that depends upon the MIONP distribution. Intratumour heat conduction resulting from this balance of (constant power) heat generated by MIONPs and depleted heat was treated analytically and experimentally by Andrä et al. [47] and later confirmed by others [54,55,66].

Constant power mNPH results obtained in this study using PC3 and LAPC-4 tumour models, and simulations are qualitatively consistent with this description of MIONP-mediated tissue heating (Tables 3 and 4, and Figure 4A – C). Measured variations in MIONP retention (Table 1) and temperatures generated by 20-min AMF exposure at 24kA/m in PC3 tumours (Table 3) differ markedly from those measured for LAPC-4 tumours (Table 4). Only qualitative comparison of maximum measured temperature, estimated CEM43 values, and response measured by tumour growth can be made due to the inherent limitations of single-point thermometry, particularly for the PC3 tumour model. Computer simulations are thus employed to illustrate features of tumour heating that are experimentally inaccessible. The limitations of single-point thermometry are highlighted by these simulations that predict sharp thermal gradients generated by mNPH in which MIONP distribution is locally concentrated (Figure 6A and B). Nevertheless, response measured by tumour growth (Figure 4A – C) is qualitatively consistent with the measured thermometry. PC3 tumour growth following treatment appears either non-existent (70% showed no measurable growth delay compared to untreated controls) or dramatic (30% demonstrated a 4-fold increase of time to progression compared with controls) reflecting the either low or excessive thermal dose, respectively (Figure 6A and C and Table 3). By contrast, LAPC-4 tumour response appears less bifurcated with 70% showing measurable growth delay following treatment and an overall 2-fold increase of time to progression. While these responses are consistent with measured thermometry, the comparison is complicated by the different biological sensitivities to heat demonstrated by the parent cell lines (Figure 2A and B).

The limitations of variable (position-dependent) thermometry and response with mNPH arising from heterogeneous MIONP distribution has been previously described [18,53–60]. To compensate for the variable MIONP distribution and challenges it presents for thermal dosimetry, we adopted constant temperature, i.e. power modulated mNPH. The target

temperature was chosen to be between 43–44 °C, maintained for 20 min duration, and measured by single-point intratumour thermometry for all tumours. Estimated thermal doses achieved were consequently more consistent among treated cohorts of both PC3 and LAPC-4 tumours, ranging from 26 CEM43 to 34 CEM43, representing a low (mild) hyperthermia dose. These are considerably lower than thermal doses studied previously [14,15,17–24,54,58,59] to highlight potential effects of mNPH combined with RT (low dose) in two models representing varied biological sensitivities to radiation and heat (Figure 2A and B). PC3 tumour response (growth) was consistent among treated mice with power-modulated (constant thermal dose) mNPH. This contrasts with results obtained from constant power (variable thermal dose) mNPH. Response from power-modulated mNPH was also essentially indistinguishable from that of untreated controls, similar to the majority (~70%) of tumours treated with constant power mNPH, possibly recapitulating the relative thermal insensitivity of PC3 cells observed *in vitro*. Although consistent with *in vitro* data, a conclusion attributing PC3 tumour response only to inherent biological features is tenuous given the experimental limitations of the current study. Further study using constant power mNPH with increased MIONP concentration or AMF power may enhance the comparison with simulation results; however, improved thermometry will be necessary.

When used for feedback control of power, single-point intratumour thermometry can limit comprehensive thermal doses (i.e. CEM43T90) to below therapeutic values for low-dose mNPH with heterogeneous MIONP distributions. Heat generated by the MIONPs conducts away from the heating zones containing high MIONP concentrations to generate intense local thermal gradients. If located within an intense heating zone, a temperature sensor providing the feedback for power control will initiate premature power reductions to maintain heating within predetermined limits. Consequently, power deposited will be insufficient to generate thermal gradients needed to encompass adequate tumour volume (90%). This effect is demonstrated with a simple two-dimensional simulation of tumour heating in which power-modulated mNPH is explored with variable temperature sensor positioning (Figure 7A–C). In this context, a uniform MIONP intratumour distribution is superior to localised and heterogeneous MIONP deposits. LAPC-4 tumours present an interesting comparative model to the PC3 tumours. MIONP distribution is heterogeneous with local MIONP concentrations that seem to be more uniformly distributed throughout the tumour. In one sense, this model may present the truly ideal MIONP distribution – local high concentrations of MIONPs distributed throughout the tumour that can create localised heating zones from which heat conducts to merge with heat created by neighbouring zones. Heat flux (rate of loss) at the tumour–tissue boundary may be less than that encountered with perfectly uniform MIONP distribution, thus potentially generating a more uniform thermal distribution within the tumour.

Only when the temperature sensor is placed at or near the tumour–tissue boundary does the 2-D simulation predict that minimal CEM43T90 doses can be achieved (Figure 7A–C). mNPH with temperature monitoring and feedback localised to tumour–tissue boundary is more likely to achieve a minimal CEM43T90, compensating for heterogeneous intratumour MIONP distribution. Of course, power modulation with a heterogeneous and locally concentrated MIONP distribution will likely produce much higher intratumour temperatures

to achieve the required tumour–tissue boundary temperature. Such high (localised) intratumour thermal doses may produce local tissue necrosis or ablation that may influence outcomes with combined therapy. An additional consideration is the effect of hypoxic and necrotic regions of tumours on both heating properties and response to radiation therapy. Tumours encountered in both preclinical and clinical settings often exhibit such heterogeneity. Regions of hypoxia and necrosis are typically less sensitive to radiation than surrounding normoxic tissues. Consequences to heat transfer and response of such regions to mNPH and radiation therapy can prove interesting with potential significant benefit that merits investigation. The simulations suggest, with appropriate caveats, that temperature monitoring at the tumour–tissue interface is necessary to ensure a minimally effective thermal distribution (CEM43T90).

When mNPH was combined with RT, response of both PC3 and LAPC-4 tumours was improved when compared against either controls or single-agent therapy given at a similar dose. Response measured for PC3 tumours, however, was modest, again reflecting the trends observed *in vitro*. LAPC-4 tumours demonstrated a more pronounced response, essentially equivalent to response from 8 Gy RT, to combinatorial therapy (Figure 5B). These results are tantalising, but further investigation is needed to explore the nature of the distinct response to radiation and heat therapies displayed by PC3 and LAPC-4 cells and tumours. Additional studies are also needed to explore variable dose and treatment schedule (fractionated) combinations, and effects of mNPH ± RT on tumours having variable size. The present work limits the study to tumours having limited and small (~150 mm^3) volume, yet locally advanced disease (by definition) represents large tumours. The simulations seem to present a consistent pattern of predictions with experimental results; however, conclusions should be limited to suggestive comparisons. While the simplicity of the model, i.e. 2D with constant perfusion, highlighted certain features of the physics of nanoparticle hyperthermia, further simulations with more realistic parameters and constraints are necessary.

To summarise, we investigated the effects of RT, HT, and one combination of these in several model systems: (1) *in vitro* cell culture with two human prostate cancer cell lines, PC3 and LAPC-4; (2) *in vivo* mouse models of subcutaneous PC3 and LAPC-4 tumours; and, (3) '*in silico*' 2-D simulation model of MIONP heating with concentrated (PC3) and uniform (LAPC-4) MIONP intratumour distributions. Following percutaneous injection of MIONP suspensions, PC3 and LAPC-4 tumours displayed different patterns of intratumour MIONP distribution and retention, providing a biological model to explore effects of MIONP distribution for mNPH, RT, and combined low-dose mNPH+RT. While responses were generally consistent with measured thermometry and inherent biological sensitivity of parent cells to the effects of HT and RT, and these results were generally consistent with simulations, further study is needed to elucidate the relative influence of multiple parameters made possible with mNPH. Each of the models used in this study offers select advantages to highlight particular features of biology or mechanics of heat transfer; and, simultaneously each model possesses significant limitations requiring a careful comparative examination among the results. Inherent biological sensitivity demonstrated by LAPC-4 cells relative to PC3 cells to the effects of RT, HT, and RT + HT introduce a confounding element that

motivates further study. Taken together, however, the results consistently suggest that limitations of mNPH due to heterogeneous intratumour MIONP distributions and single-point thermometry may be overcome by modulating AMF power with carefully positioned temperature feedback control. We might thus speculate that knowledge of nanoparticle distribution, as obtained by imaging, can be combined with computational modelling of the heating process to guide both temperature sensor placement and power modulation to realise patient-specific hyperthermia treatment.

Conclusions

Complementary biological damage caused by heat and ionising radiation offers significant potential to enhance clinical management of locally advanced and aggressive cancer. Widespread adoption of hyperthermia is inhibited by challenges to target, measure, and control heat deposition in tumours sufficient to achieve adequate thermal dose and distribution. The potential offered by magnetic iron oxide nanoparticles that generate heat when exposed to alternating magnetic fields has been partially eclipsed by unique challenges to consistently achieve appropriate nanoparticle distributions within a tumour. Results presented from studies of two prostate cancer xenograft mouse tumour models and computer simulations suggest that these limitations may be overcome by modulating magnetic field parameters with appropriate temperature feedback control.

Acknowledgments

This work was funded by an award from the Safeway Foundation and the Prostate Cancer Foundation, and by a donation from David H. Koch. ICP-MS work was supported in part by the Maryland Cigarette Restitution Fund Program at Johns Hopkins Bloomberg School of Public Health and the NIEHS Center, P30 ES00319. The authors alone are responsible for the content and writing of the paper. Partial support for S. K. Kandala and C. Herman was provided by the National Institutes of Health, NCI Grant No. R01CA161265. Additional support for animal facilities at the Sidney Kimmel Comprehensive Cancer Center was provided by the NCI/NIH P30 CA006973.

References

1. Sanda MG, Dunn RL, Michalski J, Sandler HM, Northouse L, Hembroff L, et al. Quality of life and satisfaction with outcome among prostate-cancer survivors. New Engl J Med. 2008; 358:1250–1261. [PubMed: 18354103]
2. Sundi D, Jeong BC, Lee SB, Han M. Optimizing the management of high-risk, localized prostate cancer. Korean J Urol. 2012; 53:815–820. [PubMed: 23301123]
3. Khor R, Williams S. Contemporary issues in radiotherapy for clinically Localized prostate cancer. Hematol Oncol Clin N Am. 2013; 27:1137–1162.
4. Citrin D, Camphausen KA. Biomarkers for prostate cancer: Who will benefit from local treatment, who harbors occult systemic disease and who needs treatment at all? Biomark Med. 2013; 7:823–825. [PubMed: 24266814]
5. Horsman MR, Overgaard J. Hyperthermia: A potent enhancer of radiotherapy. Clin Oncol. 2007; 19:418–426.
6. Krawczyk PM, Eppink B, Essers J, Stap J, Rodermond H, Odijk H, et al. Mild hyperthermia inhibits homologous recombination, induces BRCA2 degradation, and sensitizes cancer cells to poly (ADP-ribose) polymerase-1 inhibition. Proc Natl Acad Sci. 2011; 108:9851–9856. [PubMed: 21555554]
7. Triantopoulou S, Efstathopoulos E, Platoni K, Uzunoglou N, Kelekis N, Kouloulias V. Radiotherapy in conjunction with superficial and intracavitary hyperthermia for the treatment of solid tumors: Survival and thermal parameters. Clin Transl Oncol. 2013; 15:95–105. [PubMed: 23180345]

8. Bergs JW, Krawczyk PM, Borovski T, ten Cate R, Rodermond HM, Stap J, et al. Inhibition of homologous recombination by hyperthermia shunts early double strand break repair to non-homologous end-joining. DNA Repair. 2013; 12:38–45. [PubMed: 23237939]

9. Tuul M, Kitao H, Iimori M, Matsuoka K, Kiyonari S, Saeki H, et al. Rad9, Rad17, TopBP1 and claspin play essential roles in heat-induced activation of ATR kinase and heat tolerance. PloS One. 2013; 8:e55361. [PubMed: 23383325]

10. Pankhurst Q, Thanh N, Jones S, Dobson J. Progress in applications of magnetic nanoparticles in biomedicine. J Phys D Appl Phys. 2009; 42:224001.

11. Ivkov R. Magnetic nanoparticle hyperthermia: A new frontier in biology and medicine? Int J Hyperthermia. 2013; 29:703–705. [PubMed: 24219798]

12. Dennis CL, Ivkov R. Physics of heat generation using magnetic nanoparticles for hyperthermia. Int J Hyperthermia. 2013; 29:715–729. [PubMed: 24131317]

13. Gilchrist RK, Medal R, Shorey WD, Hanselman RC, Parrott JC, Taylor CB. Selective inductive heating of lymph nodes. Ann Surg. 1957; 146:596–606. [PubMed: 13470751]

14. Maier-Hauff K, Rothe R, Scholz R, Gneveckow U, Wust P, Thiesen B, et al. Intracranial thermotherapy using magnetic nanoparticles combined with external beam radiotherapy: Results of a feasibility study on patients with glioblastoma multiforme. J Neuro-Oncol. 2007; 81:53–60.

15. Maier-Hauff K, Ulrich F, Nestler D, Niehoff H, Wust P, Thiesen B, et al. Efficacy and safety of intratumoral thermotherapy using magnetic iron-oxide nanoparticles combined with external beam radiotherapy on patients with recurrent glioblastoma multiforme. J Neuro-Oncol. 2011; 103:317–324.

16. Zadnik PL, Molina CA, Sarabia-Estrada R, Groves ML, Wabler M, Mihalic J, et al. Characterization of intratumor magnetic nanoparticle distribution and heating in a rat model of metastatic spine disease. J Neurosurg Spine. 2014; 20:740–750. [PubMed: 24702509]

17. Johannsen M, Gneueckow U, Thiesen B, Taymoorian K, Cho CH, Waldofner N, et al. Thermotherapy of prostate cancer using magnetic nanoparticles: Feasibility, imaging, and three-dimensional temperature distribution. Eur Urol. 2007; 52:1653–1662. [PubMed: 17125906]

18. Johannsen M, Gneveckow U, Taymoorian K, Thiesen B, Waldofner N, Scholz R, et al. Morbidity and quality of life during thermotherapy using magnetic nanoparticles in locally recurrent prostate cancer: Results of a prospective phase I trial. Int J Hyperther. 2007; 23:315–323.

19. Johannsen M, Thiesen B, Wust P, Jordan A. Magnetic nanoparticle hyperthermia for prostate cancer. Int J Hyperthermia. 2010; 26:790–795. [PubMed: 20653418]

20. Johannsen M, Gneveckow U, Eckelt L, Feussner A, Waldofner N, Scholz R, et al. Clinical hyperthermia of prostate cancer using magnetic nanoparticles: Presentation of a new interstitial technique. Int J Hyperthermia. 2005; 21:637–647. [PubMed: 16304715]

21. Dennis CL, Jackson AJ, Borchers JA, Hoopes PJ, Strawbridge R, Foreman AR, et al. Nearly complete regression of tumors via collective behavior of magnetic nanoparticles in hyperthermia. Nanotechnology. 2009; 20:395103. [PubMed: 19726837]

22. Giustini AJ, Ivkov R, Hoopes PJ. Magnetic nanoparticle biodistribution following intratumoral administration. Nanotechnology. 2011; 22:345101. [PubMed: 21795772]

23. DeNardo SJ, DeNardo GL, Miers LA, Natarajan A, Foreman AR, Gruettner C, et al. Development of tumor targeting bioprobes (In-111-chimeric L6 monoclonal antibody nanoparticles) for alternating magnetic field cancer therapy. Clin Cancer Res. 2005; 11:S7087–S7092.

24. DeNardo SJ, DeNardo GL, Natarajan A, Miers LA, Foreman AR, Gruettner C, et al. Thermal dosimetry predictive of efficacy of In-111-ChL6 nanoparticle AMF-induced thermoablative therapy for human breast cancer in mice. J Nucl Med. 2007; 48:437–444. [PubMed: 17332622]

25. Dewhirst, M.; Das, S.; Stauffer, P.; Craciunescu, O.; Vujaskovic, Z.; Thrall, D. Clinical Radiation Oncology. 3rd ed.. Elsevier: Philadelphia, PA; 2011. Hyperthermia; p. 385-403.

26. Jones EL, Oleson JR, Prosnitz LR, Samulski TV, Vujaskovic Z, Yu DH, et al. Randomized trial of hyperthermia and radiation for superficial tumors. J Clin Oncol. 2005; 23:3079–3085. [PubMed: 15860867]

27. Mitsumori M, Hiraoka M, Shibata T, Okuno Y, Nagata Y, Nishimura Y, et al. Targeted hyperthermia using dextran magnetite complex: A new treatment modality for liver tumors. Hepato-Gastroenterol. 1996; 43:1431–1437.

28. Moroz P, Jones SK, Winter J, Gray BN. Targeting liver tumors with hyperthermia: Ferromagnetic embolization in a rabbit liver tumor model. J Surg Oncol. 2001; 78:22–29. [PubMed: 11519064]
29. Moroz P, Pardoe H, Jones SK, St Pierre TG, Song S, Gray BN. Arterial embolization hyperthermia: Hepatic iron particle distribution and its potential determination by magnetic resonance imaging. Phys Med Biol. 2002; 47:1591–1602. [PubMed: 12043822]
30. Wabler M, Zhu WL, Hedayati M, Attaluri A, Zhou HM, Mihalic J, et al. Magnetic resonance imaging contrast of iron oxide nanoparticles developed for hyperthermia is dominated by iron content. Int J Hyperthermia. 2014; 30:192–200. [PubMed: 24773041]
31. Bordelon DE, Cornejo C, Gruttner C, Westphal F, DeWeese TL, Ivkov R. Magnetic nanoparticle heating efficiency reveals magneto-structural differences when characterized with wide ranging and high amplitude alternating magnetic fields. J Appl Phys. 2011; 109:124904.
32. Grüttner C, Müller K, Teller J, Westphal F, Foreman A, Ivkov R. Synthesis and antibody conjugation of magnetic nanoparticles with improved specific power absorption rates for alternating magnetic field cancer therapy. J Magn Magn Mater. 2007; 311:181–186.
33. Dennis CL, Jackson AJ, Borchers JA, Ivkov R, Foreman AR, Lau JW, et al. The influence of collective behavior on the magnetic and heating properties of iron oxide nanoparticles. J Appl Phys. 2008; 103:07A319.
34. Clark JD, Gebhart GF, Gonder JC, Keeling ME, Kohn DF. The 1996 Guide for the Care and Use of Laboratory Animals. ILAR J. 1997; 38:41–48. [PubMed: 11528046]
35. Kut C, Zhang Y, Hedayati M, Zhou H, Cornejo C, Bordelon DE, et al. Preliminary study of injury from heating systemically delivered, nontargeted dextran-superparamagnetic iron oxide nanoparticles in mice. Nanomedicine. 2012; 7:1697–1711. [PubMed: 22830502]
36. Bordelon DE, Goldstein RC, Nemkov VS, Kumar A, Jackowski JK, DeWeese TL, et al. Modified solenoid coil that efficiently produces high amplitude AC magnetic fields with enhanced uniformity for biomedical applications. IEEE Trans Magn. 2012; 48:47–52. [PubMed: 25392562]
37. Kumar A, Attaluri A, Mallipudi R, Cornejo C, Bordelon D, Armour M, et al. Method to reduce non-specific heating of small animals in solenoid coils. Int J Hyperthermia. 2013; 29:106–120. [PubMed: 23402327]
38. Wong J, Armour E, Kazanzides P, Iordachita U, Tryggestad E, Deng H, et al. High-resolution, small animal radiation research platform with X-ray tomographic guidance capabilities. Int J Radiat Oncol. 2008; 71:1591–1599.
39. Sapareto SA, Dewey WC. Thermal dose determination in cancer therapy. Int J Radiat Oncol. 1984; 10:787–800.
40. Tompkins D, Vanderby R, Klein S, Beckman W, Steeves R, Frye D, et al. Temperature-dependent versus constant-rate blood perfusion modelling in ferromagnetic thermoseed hyperthermia: Results with a model of the human prostate. Int J Hyperthermia. 1994; 10:517–536. [PubMed: 7963808]
41. Pennes HH. Analysis of tissue and arterial blood temperatures in the resting human forearm. J Appl Physiol. 1998; 85:5–34. [PubMed: 9714612]
42. Hasgall, P.; Neufeld, E.; Gosselin, M.; Klingenböck, A.; Kuster, N. IT'IS database for thermal and electromagnetic parameters of biological tissues. 2011 Sep 26th. http://www.itis.ethz.ch/itis-for-health/tissue-properties/overview/
43. Buckley DL, Roberts C, Parker GJ, Logue JP, Hutchinson CE. Prostate Cancer: Evaluation of vascular characteristics with dynamic contrast-enhanced T1-weighted MR imaging - Initial experience 1. Radiology. 2004; 233:709–715. [PubMed: 15498903]
44. Çetingül MP, Herman C. A heat transfer model of skin tissue for the detection of lesions: Sensitivity analysis. Phys Med Biol. 2010; 55:5933. [PubMed: 20858919]
45. Duck, FA. Physical properties of tissues: A comprehensive reference book. San Diego, CA: Academic Press; 1990.
46. Torvi D, Dale J. A finite element model of skin subjected to a flash fire. J Biomechanical Eng. 1994; 116:250–255.
47. Andra W, d'Ambly CG, Hergt R, Hilger I, Kaiser WA. Temperature distribution as function of time around a small spherical heat source of local magnetic hyperthermia. J Magn Magn Mater. 1999; 194:197–203.

48. Russell, PJ.; Kingsley, EA. Human prostate cancer cell lines. In: Russell, PJ.; Jackson, P.; Kingsley, EA., editors. Prostate Cancer Methods and Protocols. Totowa, NJ: Humana Press; 2003. p. 21-39.

49. Taylor BS, Schultz N, Hieronymus H, Gopalan A, Xiao Y, Carver BS, et al. Integrative genomic profiling of human prostate cancer. Cancer Cell. 2010; 18:11–22. [PubMed: 20579941]

50. Tai S, Sun Y, Squires JM, Zhang H, Oh WK, Liang CZ, et al. PC3 is a cell line characteristic of prostatic small cell carcinoma. Prostate. 2011; 71:1668–1679. [PubMed: 21432867]

51. Baronzio, GF.; Hager, ED. Hyperthermia in Cancer Treatment: A Primer. New York, NY: Landes Bioscience; 2008.

52. Kossatz S, Ludwig R, Dähring H, Ettelt V, Rimkus G, Marciello M, et al. High therapeutic efficiency of magnetic hyperthermia in xenograft models achieved with moderate temperature dosages in the tumor area. Pharm Res. 2014; 32:3274–3288. [PubMed: 24890197]

53. Rodrigues HF, Mello FM, Branquinho LC, Zufelato N, Silveira-Lacerda EP, Bakuzis AF. Real-time infrared thermography detection of magnetic nanoparticle hyperthermia in a murine model under a non-uniform field configuration. Int J Hyperthermia. 2013; 29:752–767. [PubMed: 24138472]

54. Attaluri A, Ma RH, Qiu Y, Li W, Zhu L. Nanoparticle distribution and temperature elevations in prostatic tumours in mice during magnetic nanoparticle hyperthermia. Int J Hyperthermia. 2011; 27:491–502. [PubMed: 21756046]

55. Johannsen M, Thiesen B, Gneveckow U, Taymoorian K, Waldofner N, Scholz R, et al. Thermotherapy using magnetic nanoparticles combined with external radiation in an orthotopic rat model of prostate cancer. Prostate. 2006; 66:97–104. [PubMed: 16114060]

56. Johannsen M, Thiesen B, Jordan A, Taymoorian K, Gneveckow U, Waldofner N, et al. Magnetic fluid hyperthermia (MFH) reduces prostate cancer growth in the orthotopic Dunning R3327 rat model. Prostate. 2005; 64:283–292. [PubMed: 15726645]

57. Attaluri A, Ivkov R, Ma R, Zhu L. Nanoparticle redistribution during magnetic nanoparticle hyperthermia: Multi-physics porous medium model analyses. ASME 2012 International Mechanical Engineering Congress and Exposition. American Society of Mechanical Engineers, Houston, TX. 2012

58. Du LH, Zhou JM, Wang XW, Sheng L, Wang GH, Xie XX, et al. Effect of local hyperthermia induced by nanometer magnetic fluid on the rabbit VX2 liver tumor model. Prog Nat Sci. 2009; 19:1705–1712.

59. Jordan A, Scholz R, Wust P, Fahling H, Krause J, Wlodarczyk W, et al. Effects of magnetic fluid hyperthermia (MFH) on C3H mammary carcinoma in vivo. Int J Hyperthermia. 1997; 13:587–605. [PubMed: 9421741]

60. Wust P, Gneveckow U, Johannsen M, Böhmer D, Henkel T, Kahmann F, et al. Magnetic nanoparticles for interstitial thermo-therapy-feasibility, tolerance and achieved temperatures. Int J Hyperthermia. 2006; 22:673–685. [PubMed: 17390997]

61. Sawyer CA, Habib AH, Miller K, Collier KN, Ondeck CL, McHenry ME. Modeling of temperature profile during magnetic thermotherapy for cancer treatment. J Appl Phys. 2009; 105:07B320.

62. Pavel M, Stancu A. Study of the optimum injection sites for a multiple metastases region in cancer therapy by using MFH. IEEE Trans Magn. 2009; 45:4825–4828.

63. Xu R, Yu H, Zhang Y, Ma M, Chen Z, Wang C, et al. Three-dimensional model for determining inhomogeneous thermal dosage in a liver tumor during arterial embolization hyperthermia incorporating magnetic nanoparticles. IEEE Trans Magn. 2009; 45:3085–3091.

64. Mital M, Tafreshi HV. A methodology for determining optimal thermal damage in magnetic nanoparticle hyperthermia cancer treatment. Int J Num Methods Biomed Eng. 2012; 28:205–213.

65. Fasla B, Benmouna R, Benmouna M. Modeling of tumor's tissue heating by nanoparticles. J Appl Phys. 2010; 108:124703.

66. Dutz S, Hergt R. Magnetic nanoparticle heating and heat transfer on a microscale: Basic principles, realities and physical limitations of hyperthermia for tumour therapy. Int J Hyperthermia. 2013; 29:790–800. [PubMed: 23968194]

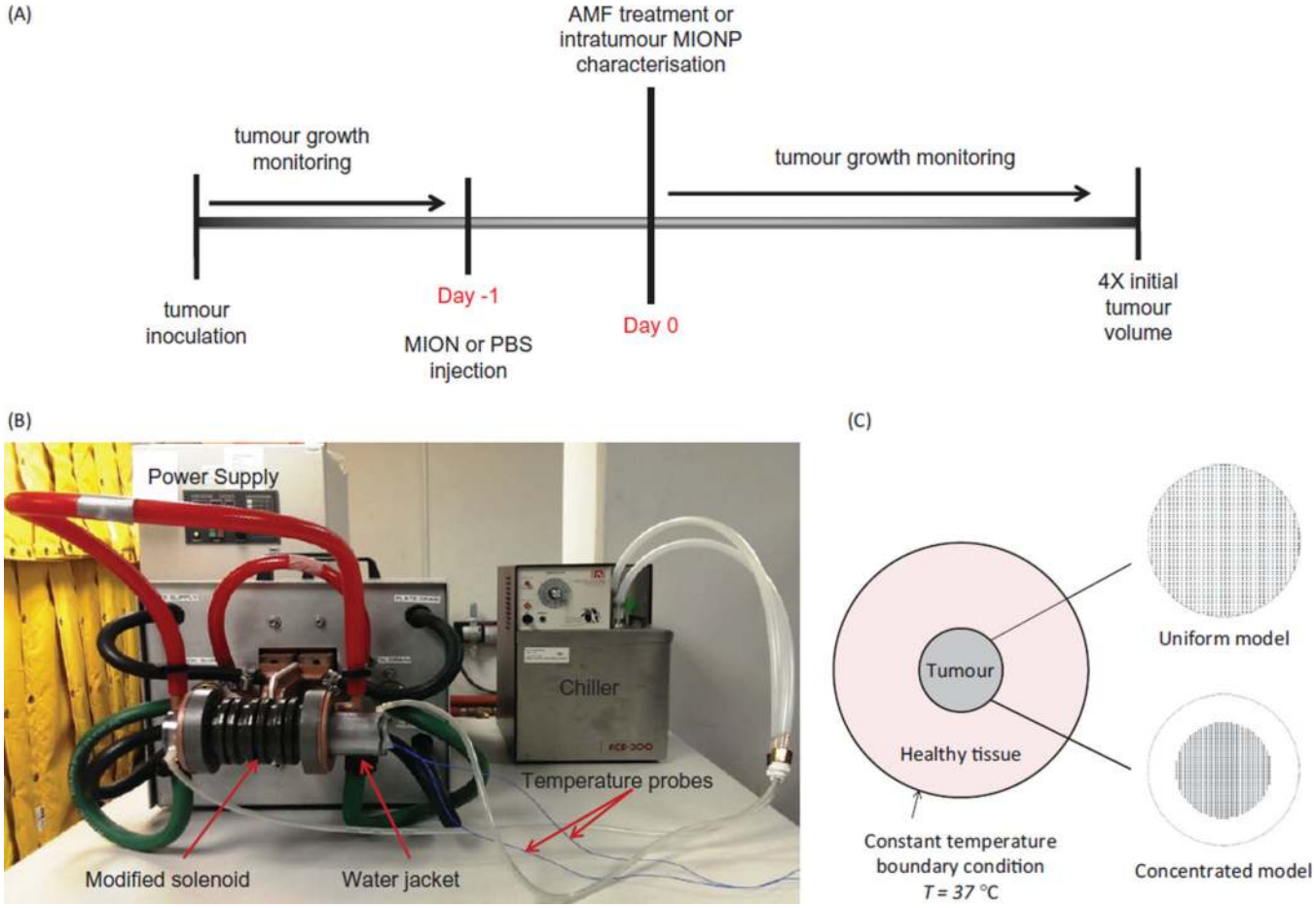

Figure 1.

(A) Schematic of the study design for therapy of either PC3 or LAPC-4 tumours in mice. (B) Photograph of experimental equipment used to perform mNPH treatments in mouse tumours. (C) Schematic of the computational model of healthy tissue and tumour with (1) uniform nanoparticle distribution, and (2) concentrated nanoparticle distribution.

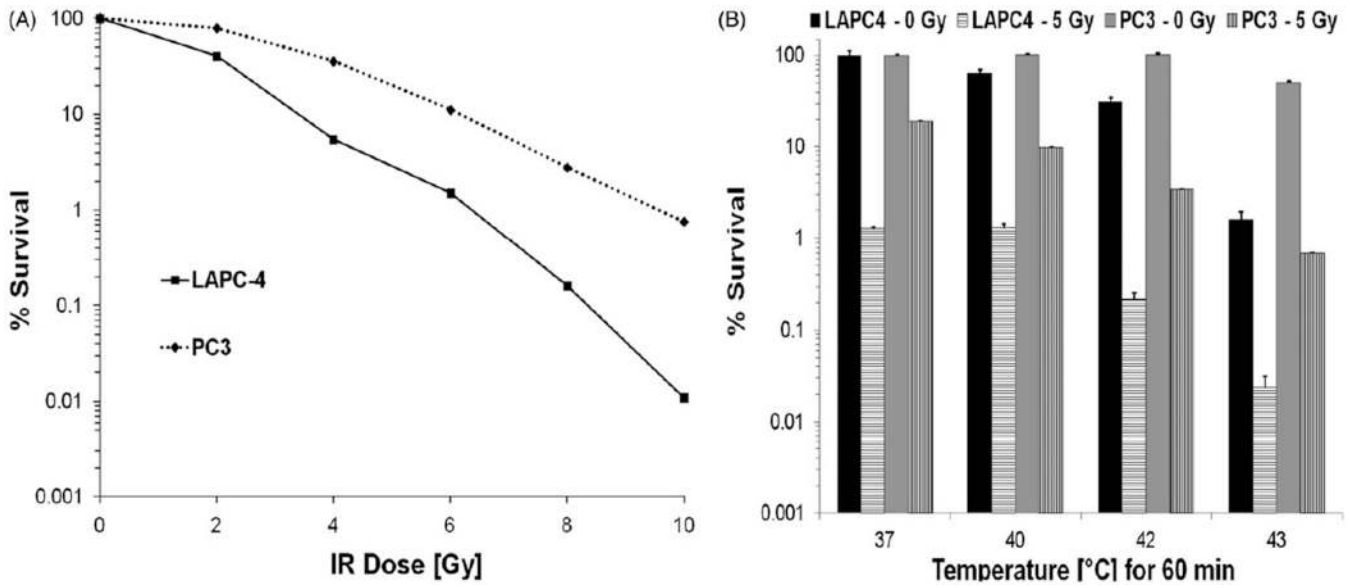

Figure 2.

(A) *In vitro* measure of surviving fraction of PC3 and LAPC-4 cells exposed to ionising radiation determined from clonogenic survival assays relative to untreated controls. Each data point represents an average of triplicate measurements. Error bars (standard error) do not appear on the log scale. (B) Surviving fraction of PC3 and LAPC-4 cells were exposed to the indicated (water bath) temperature for 60 min ± a 5-Gy dose of ionising radiation determined from clonogenic survival assays relative to untreated controls. Histogram data represent an average of triplicate measurements. Error bars represent standard error (95% CL).

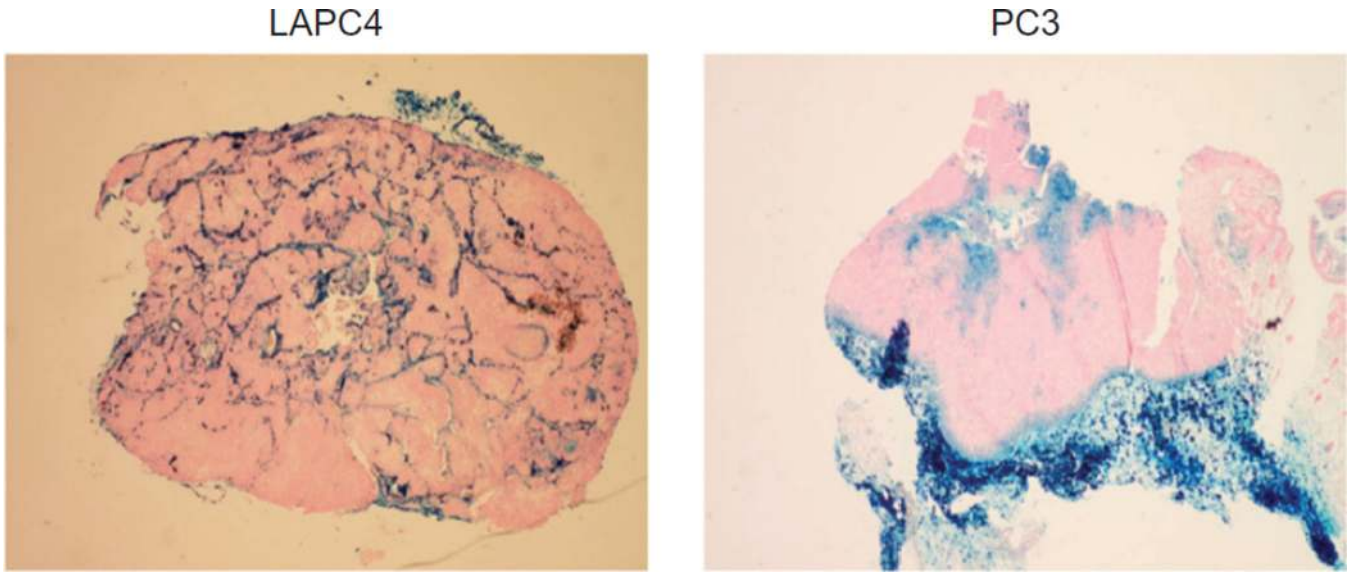

Figure 3.

Representative tumour sections harvested from mice stained with Perl's reagent (Prussian blue) highlighting iron oxide (magnetic iron oxide) distribution.

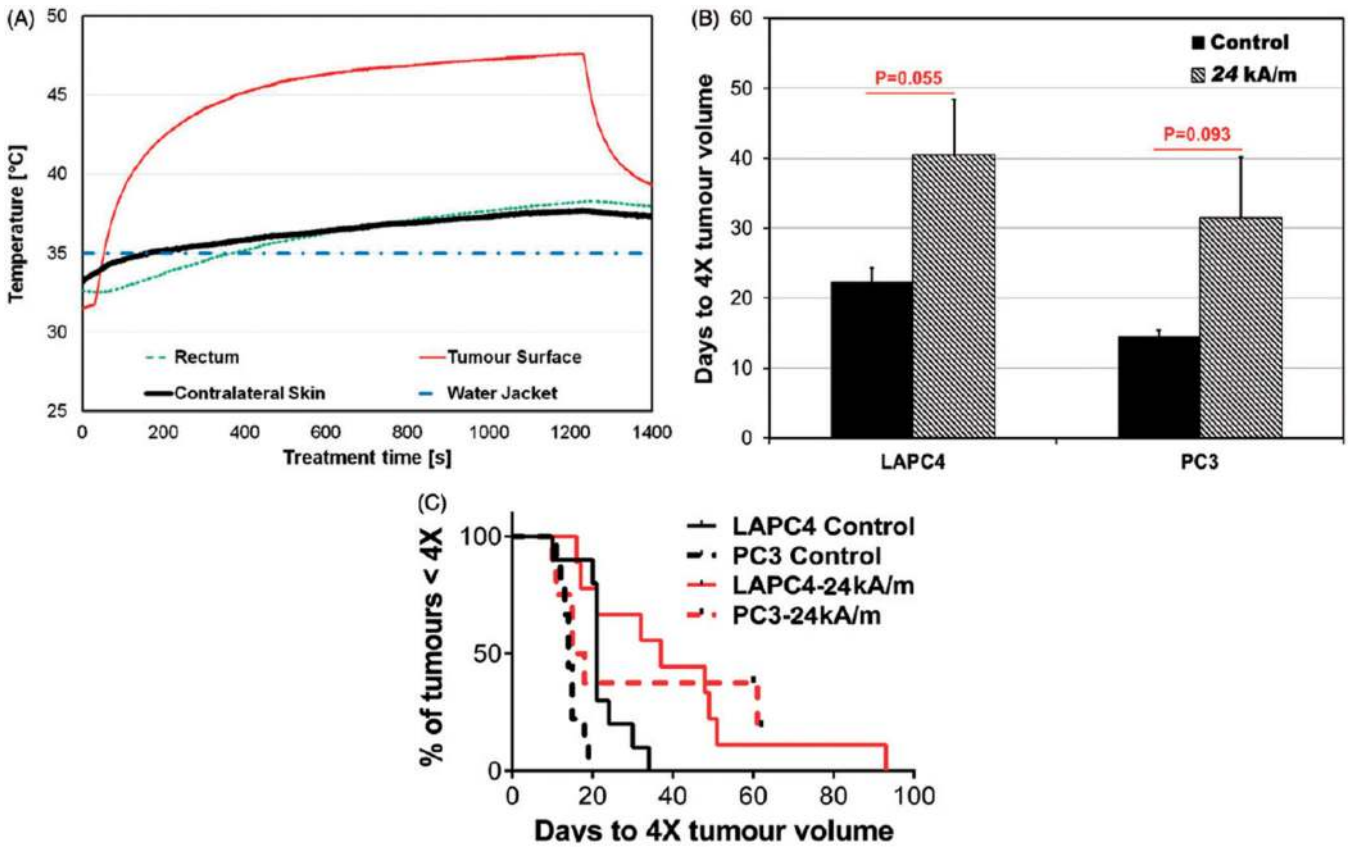

Figure 4.

(A) An example of temporal temperature rise during a constant power mNPH. (B) Histogram plot showing LAPC-4 and PC3 tumour response to constant power mNPH therapy. Bars represent mean time to progress to 4 × initial volume (at time of treatment). Tumour growth delay comparison of untreated control, and constant power mNPH, was performed using t-test with unequal variance. Two of the eight mice in the PC3-24kA/m group showed complete response (no tumour) at 60 days. For comparison purposes 60 days was considered as the time to 4 × for those two mice. (C) Kaplan-Meier plot showing the outcome of varied combinations of mNPH (constant power) for both PC3 and LAPC-4 tumours.

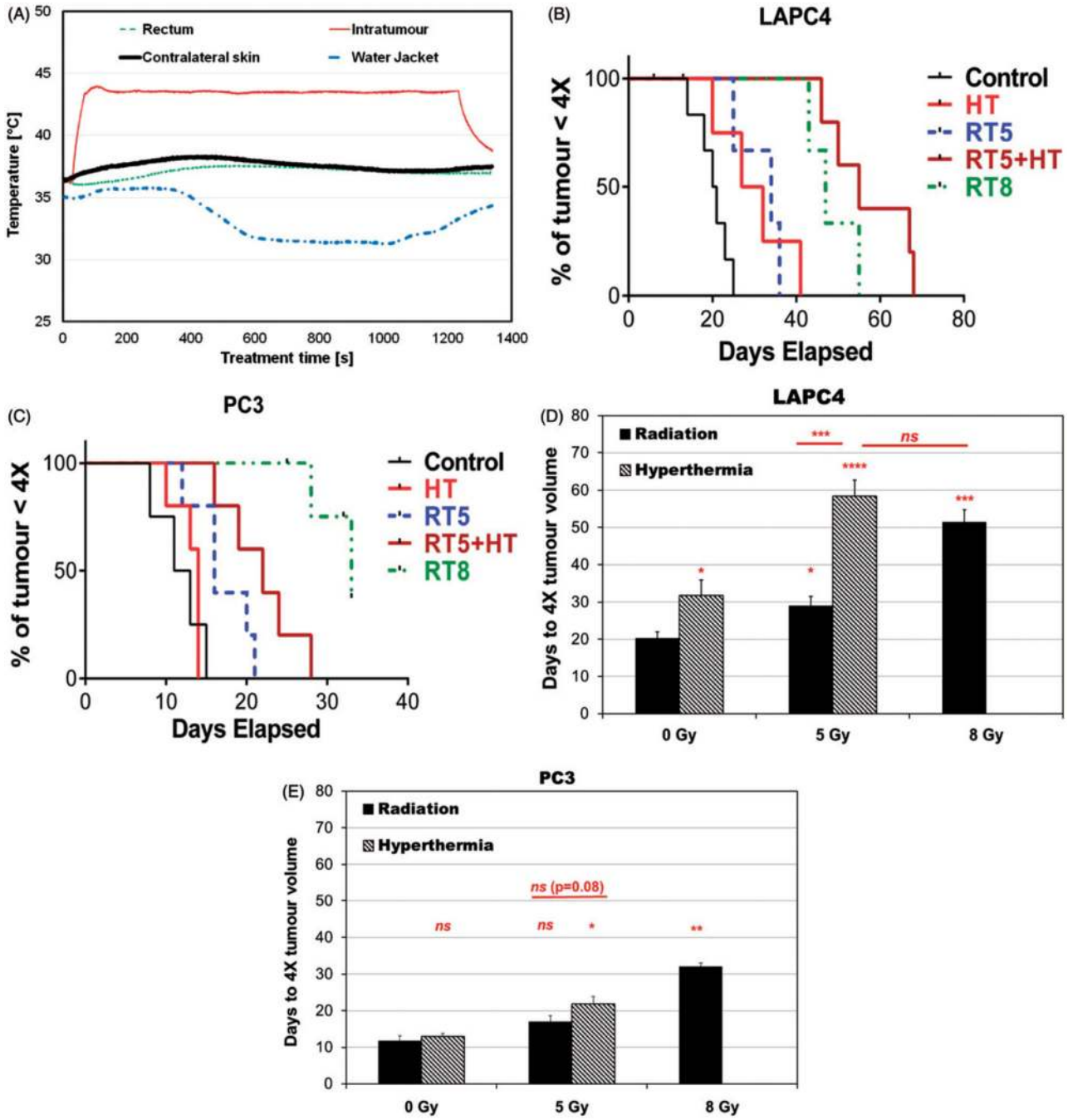

Figure 5.

(A) Representative four-point thermometry of mice treated with power-modulated mNPH. Single-point temperatures were measured at one-second intervals with optical fiber temperature probes placed into the tumour (Tumour), in a similar location subcutaneously on the opposite thigh (Contralateral) to tumour, inserted in the rectum (Rectal), and affixed to the surface of the water jacket (Water Jacket). (B) Kaplan–Meier plot summarizing outcome of power-modulated mNPH ± RT (5 Gy), and RT (RT5 and RT8) in LAPC-4 tumours. (C) As in B, but for PC3 tumours. (D) Histogram plot showing LAPC-4 tumour

response to therapy as in B. Bars represent mean time to progress to 4X initial volume (compared to time of treatment, t_0). A tumour growth delay comparison between groups was performed using *t*-test with unequal variance. (E) As in D for PC3 tumours. Key for symbols used in figures: ns $p>0.05$; *$p \leq 0.05$; **$p \leq 0.01$; ***$p \leq 0.001$; ****$p \leq 0.0001$.

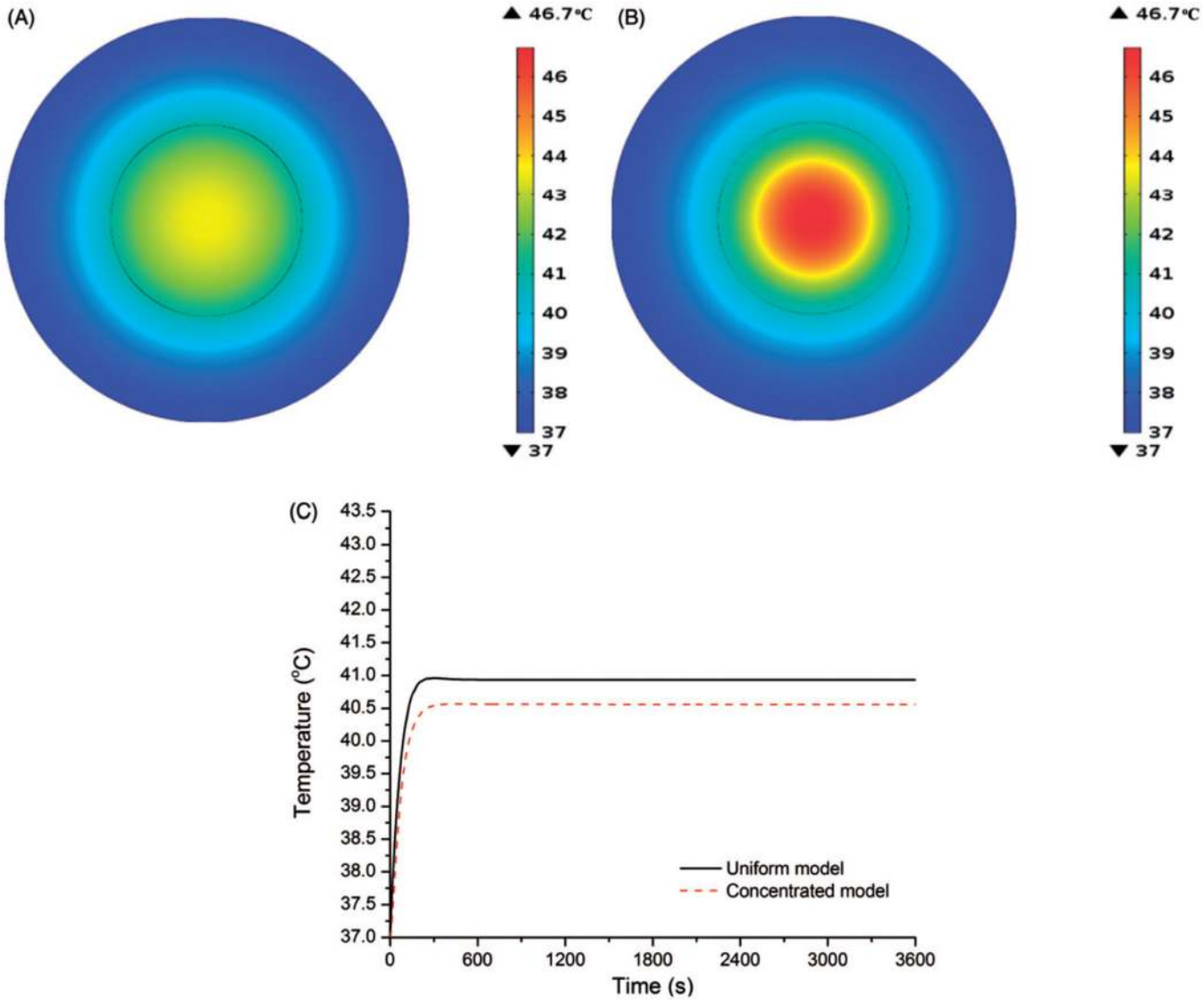

Figure 6.

(A) Temperature distribution of uniform distribution model after 60 min of heating at constant power of $Q_P = 4.6 \times 10^5$ W/m^3. (B) As in A for concentrated distribution model. (C) Variation of tumour–tissue boundary temperature with time for uniform and concentrated distribution models under heating at constant power of $Q_P = 4.6 \times 10$ W/m^3.

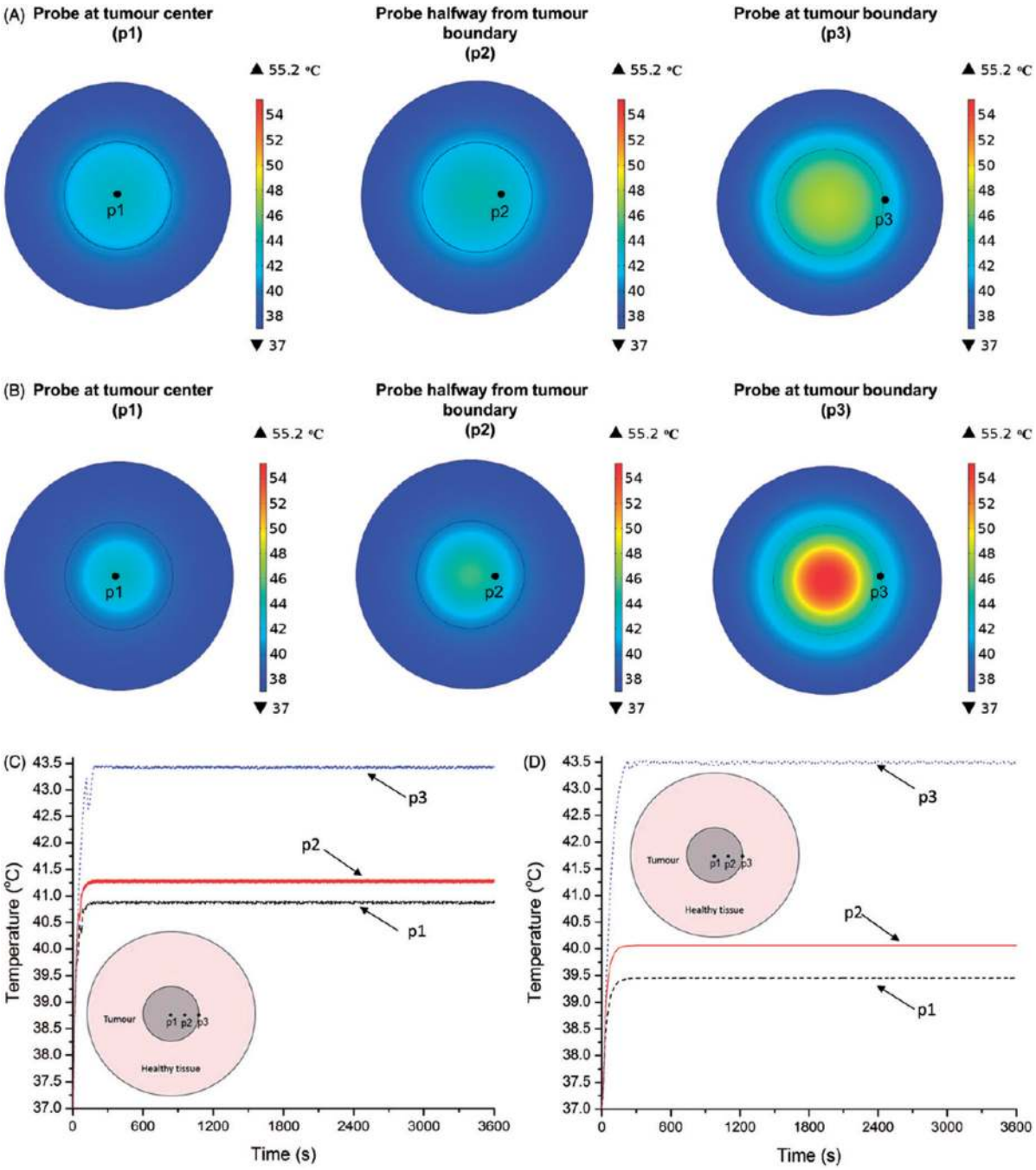

Figure 7.

(A) Temperature distribution of uniform distribution model after 60 min of heating at modulated power based on temperature feedback from (1) probe at tumour centre, (2) probe at halfway between tumour centre and tumour–tissue boundary, (3) probe at tumour–tissue boundary. (B) Same as A for concentrated model. (C) Variation of tumour–tissue boundary temperature with time for uniform distribution model under heating at modulated power based on temperature feedback from (1) at the tumour centre (Probe 1), (2) at the midpoint

between tumour centre and tumour–tissue boundary (Probe 2); and, (3) at the tumour–tissue boundary (Probe 3). (D) Same as C for concentrated model.

Table 1

Intratumour iron content measured with inductively coupled plasma mass spectrometry (ICP-MS).

	LAPC-4 (n = 5)*			PC3 (n = 4)*		
	Injected (μg Fe)	**Measured (μg Fe)**	**% Fe Retained**	**Injected (μg Fe)**	**Measured (μg Fe)**	**% Fe Retained**
Mean	830	654	79	771	423	55
SE	16	61	6	36	93	13
Median	825	632	79	745	417	51
Minimum	798	493	58	718	225	30
Maximum	878	867	99	878	634	88

* Measured Fe in control samples injected with PBS for LAPC-4 (n=5) and PC3 (n=3) were 8±2μg Fe and 11±1μg Fe respectively. SE, Standard error.

Table 2

Thermophysical properties of tumour and healthy tissue.

	Density ρ (kg/m^3)	Specific heat c (J/kg K)	Thermal conductivity k (W/m K)	Blood perfusion rate ϖ (1/s)	Metabolic heat generation rate Q_m (W/m^3)
Tumour	1045 [40]	3760 [40]	0.51 [40]	0.0095 [41]	31872.5 [42]
Healthy tissue	1045 [40]	3760 [40]	0.51 [40]	0.003 [4]	6374.5 [40]
Blood*	1060 [43]	N/A	3770 [44]	N/A	N/A

* Temperature of blood (T_b) was fixed at 37 °C [7]. N/A, not applicable.

Table 3

Single-point intratumour thermometry of mNPH in PC3 tumours and estimated thermal dose.

PC3	
$T_{max\ tumour}$ (°C)	CEM43 °C_{tumour}
44.5	11
45.9	42
47.6	210
50.1	N/A (>1000)
52.2	N/A (>1000)
54.8	N/A (>1000)

N/A, not applicable.

Table 4

Single-point tumour surface thermometry of mNPH in LAPC-4 tumours and estimated thermal dose.

LAPC-4	
$T_{max\ surface}$ (°C)	CEM43 °$C_{surface}$
37.3	<1
40.7	<1
40.8	<1
41.7	1
44.1	15
44.2	16
45.7	63
46.9	117
47.7	218